




## Research Article

# XRD and IR revelation of a unique $g\text{-C}_3\text{N}_4$ phase with effects on collagen/hydroxyapatite bone scaffold pore geometry and stiffness



Bernard Owusu Asimeng<sup>1</sup>  · Ilayda Karadag<sup>2</sup> · Sonia Iftekhar<sup>2</sup> · Yang Xu<sup>2</sup> · Jan Czernuszka<sup>2</sup>

Received: 6 May 2020 / Accepted: 16 July 2020 / Published online: 23 July 2020

© Springer Nature Switzerland AG 2020

## Abstract

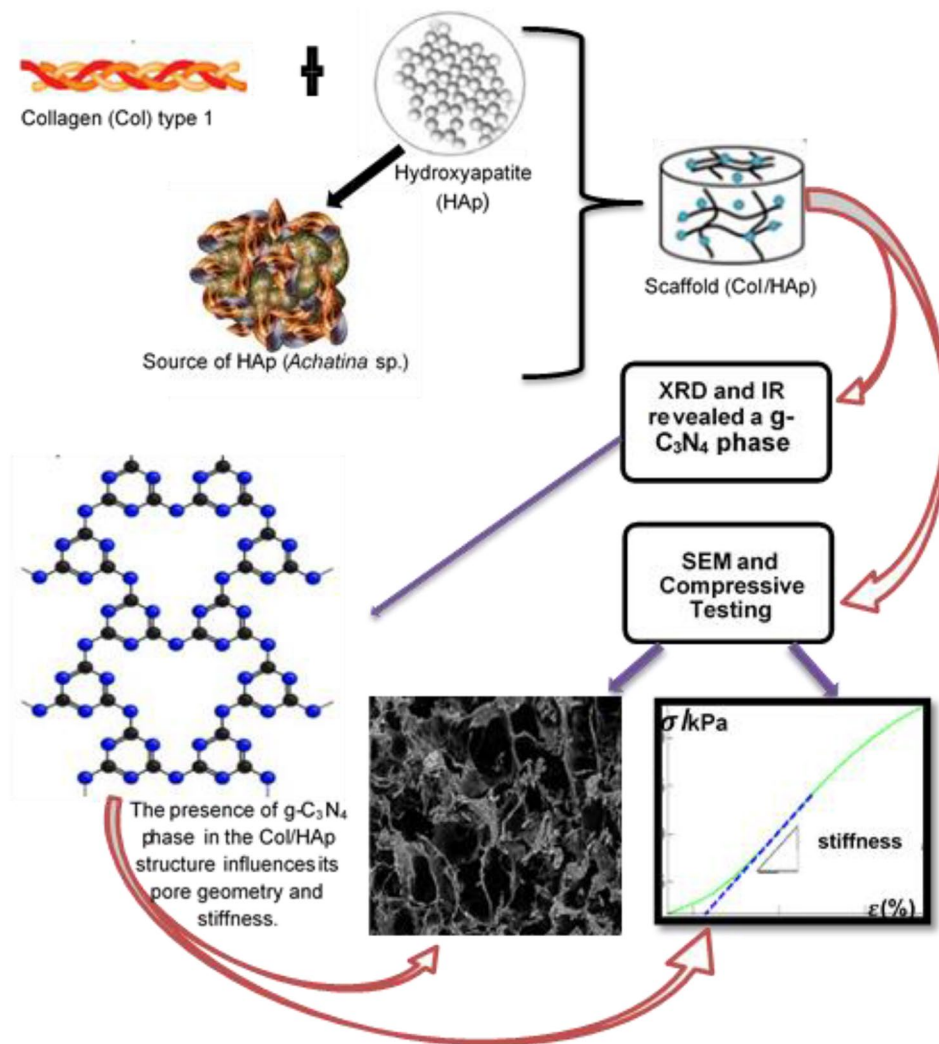
Pore geometry (pore size and pore interconnectivity) and stiffness are important design requirements for 3D-scaffold fabrication. The required pore geometry allows the passage of growth factors for cell proliferation and removal of waste products, whereas the stiffness influences attachment of osteogenic cells. This work fabricates a 3D scaffold from collagen (Col) and snail shell hydroxyapatite (HApS) and examines the influence of the HApS on the scaffold pore geometry and stiffness. The scaffolds were fabricated using freeze-drying method. Col alone and Col-commercial hydroxyapatite (Col-HApC) scaffolds were used as controls. Scanning electron microscope (SEM) reveals well-interconnected pores for Col-HApS with a mean pore size of  $246.9 \pm 68.7 \mu\text{m}$ , which was statistically ( $p < 0.05$ ) same as that of Col scaffolds  $224.4 \pm 85.7 \mu\text{m}$  and different ( $p < 0.05$ ) from Col-HApC scaffolds  $125.5 \pm 26.7 \mu\text{m}$ . Mechanical testing showed a stiffness of  $20.8 \pm 0.4 \text{ kPa}$ ,  $181.2 \pm 11.8 \text{ kPa}$ , and  $206.9 \pm 14.1 \text{ kPa}$  for Col, Col-HApC, and Col-HApS, respectively. Uniquely, X-ray diffraction (XRD) and Infrared (IR) spectroscopy of Col-HApS revealed phases and functional groups that were comparable to graphitic-like carbon nitride ( $g\text{-C}_3\text{N}_4$ ) polymeric structure. It was found that the structural change was responsible for the well-interconnected large pores and high stiffness of the scaffold. It is expected that the effect brings a wide range of functions (such as better cell attachment and nutrient transport) in the scaffold for osteogenesis. The findings indicate that Col-HApS scaffolds would promote osteogenic cell response more usefully than Col-HApC or Col scaffolds.

✉ Bernard Owusu Asimeng, boasimeng@ug.edu.gh | <sup>1</sup>Department of Biomedical Engineering, University of Ghana, Accra, Ghana. <sup>2</sup>Department of Materials, University of Oxford, Parks Road, Oxford OX1 3PH, UK.



SN Applied Sciences (2020) 2:1417 | <https://doi.org/10.1007/s42452-020-03218-8>

## Graphic abstract



**Keywords** Collagen scaffold · Hydroxyapatite · Bone regeneration · Pore size · Stiffness

## 1 Introduction

Bone tissue engineering is the field of regenerative medicine where damaged or a diseased bone is repaired by restoring new tissue using engineered scaffolds, stem cells and biomolecules [1–3]. The most successful scaffolds are fabricated from biomaterials that imitate the human extracellular matrix (ECM) more successfully [4–6]. Stem cells can be harvested from the patient's own body and seeded on the scaffold with the supply of biomolecules (nutrients) needed by the cells [7]. The scaffold should resorb controllably and be replaced by the body's own natural ECM [1, 8]. This requires a balance between the rate the scaffold

is resorbed by the cells and the rate at which the cells deposit the new ECM. Bone ECM is made up of about 30% organic component called osteoid which is mainly type 1 collagen, and 70% inorganic minerals mostly hydroxyapatite (HAp:  $\text{Ca}_{10}(\text{PO}_4)_6(\text{OH})_2$ ) with a significant amount of zinc, sodium, magnesium and carbonate [9–11].

The collagen structure is a triple helix made up of three polypeptide chains of collagen molecules (glycine, proline and hydro proline). The molecules are combined into fibrils, each of which intersects its neighbours by one-quarter of its dimension [12–14]. This creates a typical banding shape which is responsible for the tensile strength of connective tissues and bone ECM [14]. On the other hand, HAp influences the compressive modulus (stiffness) of the bone ECM [15]. The morphology of HAp is commonly reported as thin needle-like crystals which are oriented along the collagen fibrils [16]. It has

been reported that these needle-like HAp crystals in the bone scaffolds improve the stiffness and permits better cell adhesion and signaling [1, 17].

Cell proliferation also depends on the scaffold pore geometry (pore size, specific surface area and pore interconnectivity) [18]. A large specific surface area with a large volume fraction of interlinked larger pore sizes is required for effective cell permeability and nutrient transport. A critical range for pore size,  $d$  needed for the bone regeneration has been suggested to be between (50–750  $\mu\text{m}$ ) with a preference for (150–350  $\mu\text{m}$ ) [19]. If  $d$  is lower than the critical range, then cell migration is restricted due to the formation of a cellular capsule. On the other hand, a very high  $d$ , greater than the upper critical range, reduces the number of available ligand binding sites and stiffness. Therefore, sustaining a balance between the optimum pore size and specific surface area for cell adhesion and differentiation is vital for scaffold design [20]. The choice of appropriate materials to sustain a balance is a major challenge since pore volume has an inverse relation to stiffness [6]. However, researchers are incorporating minerals (like Fe, Mn) to enhance scaffold stiffness [21]. Another approach reported is the use of supermagnetic materials in scaffolds to stimulate the scaffold surface with the application of external magnetic field for better cell attachment to improve on osteogenesis [22].

In this paper, the authors used snail shell HAp to adjust the microstructure of a collagen-snail shell HAp 3D-scaffold. The adjustment revealed a new phase ( $\text{g-C}_3\text{N}_4$ : Graphitic-like Carbon Nitride) which influences both the pore geometry and stiffness. The  $\text{g-C}_3\text{N}_4$  is a layered polymeric structure usually prepared from heptazine and triazine-based molecular precursors (such as melem and melamine) [23]. The structure immense pores and suitable band gap has attracted attention in remediation and photocatalysis applications. In addition,  $\text{g-C}_3\text{N}_4$  is used as a reinforcer in polymers to improve mechanical properties in biomedical engineering for tissue scaffolds and targeted drug delivery [24]. The scaffold was produced using a freeze-drying method and characterized using x-ray diffractometry (XRD), Infrared (IR) spectroscopy, scanning electron microscope (SEM), and energy-dispersive x-ray spectrophotometer (EDS). The snail shell HAp was prepared from *Achatina achatina* (AA) shells and a phosphate containing-solution. The shells were selected because literature reports that snail shells have more carbonate, a precursor for HAp synthesis than other biogenic sources which include egg shells, corals, and fish scales [25]. Collagen (Col) alone and Col-commercial HAp scaffolds were used as controls.

## 2 Materials and methods

### 2.1 Materials

Type I collagen (Col) from bovine Achilles and commercial hydroxyapatite (HApC) were purchased from Sigma-Aldrich Ltd, UK. Snail shell hydroxyapatite (HApS) was prepared from *Achatina achatina* (AA) shells and phosphate containing-solution. The AA shells were calcined at 750 °C and the HApS was prepared using the method developed by Asimeng et al. [26].

### 2.2 Scaffolds preparation

For Col and Col-HApC scaffolds, a suspension of 100%Col and 30%Col, respectively, was prepared separately in 0.05 M acetic acid (pH 3.2) by blending in an ice bath. After blending, Col was ready for fabrication whereas for Col-HApC, 70%HApC was added immediately to the 30% Col suspension in a stepwise fashion. The pH was adjusted to 3.6 using 2 M sodium hydroxide to form a homogeneous suspension of Col-HApC. The suspension of Col and Col-HApC was pipetted into their individual moulds (polytetrafluoroethylene (PTFE)). This was frozen at  $-20\text{ }^\circ\text{C}$  and freeze dried for 24 h. The same procedure as for Col-HApC was adopted for Col-HApS fabrication.

### 2.3 HAp and scaffold characterization

X-ray diffractometer (PANalytical Empyrean, Netherlands) equipped with Cu K $\alpha$  and a wavelength of 1.5406 was used to identify the phases of HApC, HApS and scaffolds. The samples were scanned at the rate of 2° per min and the patterns were compared with Joint Committee on Powder Diffraction Standards (JCPDS) files for phase identification. Infrared (IR) (Excalibur FTS 3500 FT-IR, Varian, Inc) was used to study the functional groups. Scanning electron microscope Zeiss EVO-MA10 equipped with Oxford EDS were used to study the scaffold morphology and chemical elements present at electron high tension (EHT) of 15 kV.

### 2.4 Scaffold interconnectivity, porosity and compressive modulus

The scaffold interconnectivity was simulated using ImageJ 1.5a. SEM images were imported into the ImageJ platform and three-dimensional (3D) interactive plot selected in plugins. The scaffold porosity,  $P$ , of different groups ( $n = 10$ ) was calculated using the following gravimetric formula:

$$P = 1 - \left( \frac{\rho_{\text{scaffold}}}{\rho_{\text{material}}} \right) \quad (1)$$

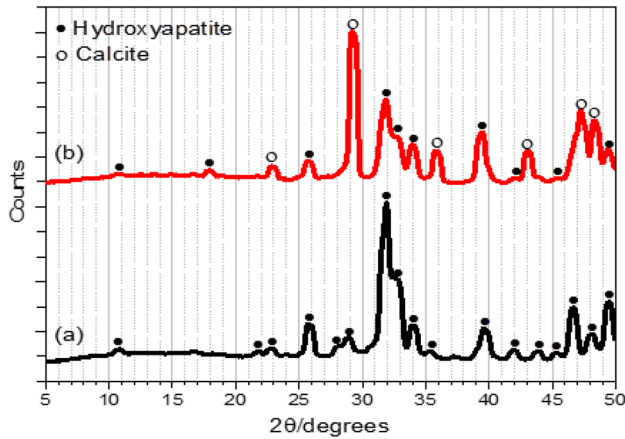


**Fig. 1** XRD patterns showing the phases of HAp **a** HApC **b** HApS. HApC shows a pure phase of HAp whereas HApS display a dual phase of hydroxyapatite and calcite

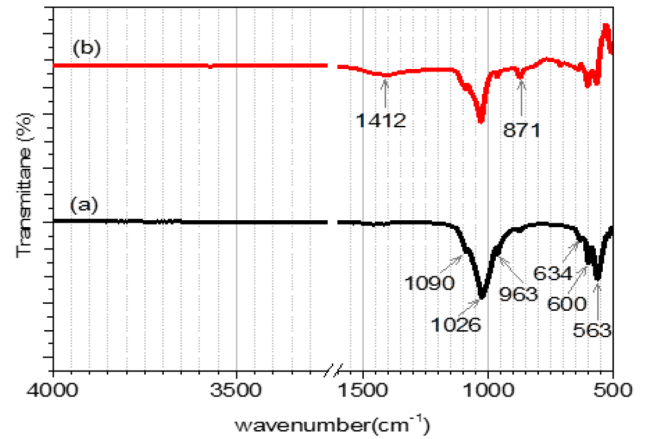


**Fig. 3** FTIR spectra displaying functional groups of hydroxyapatites **a** HApC **b** HApS. The wavenumbers 1412 and 871  $\text{cm}^{-1}$  correspond to carbonate groups and the rest of the wavenumbers are the functional groups of hydroxyapatite

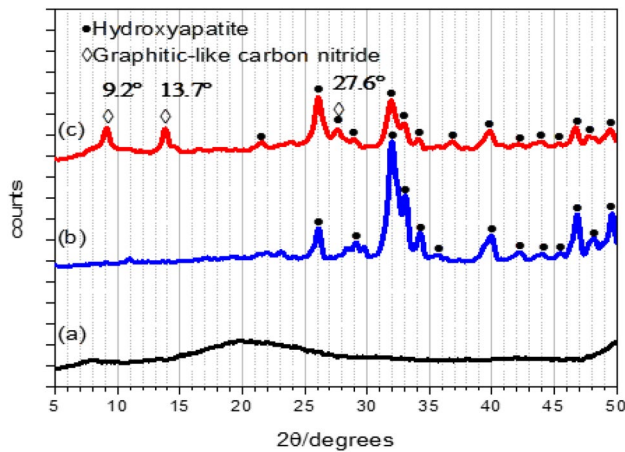


**Fig. 2** XRD patterns showing the phases of scaffolds **a** Col **b** Col-HApC **c** Col-HApS. Col and Col-HApC shows pure collagen and hydroxyapatite phases, respectively whereas Col-HApS shows hydroxyapatite and graphitic-like carbon nitride phases

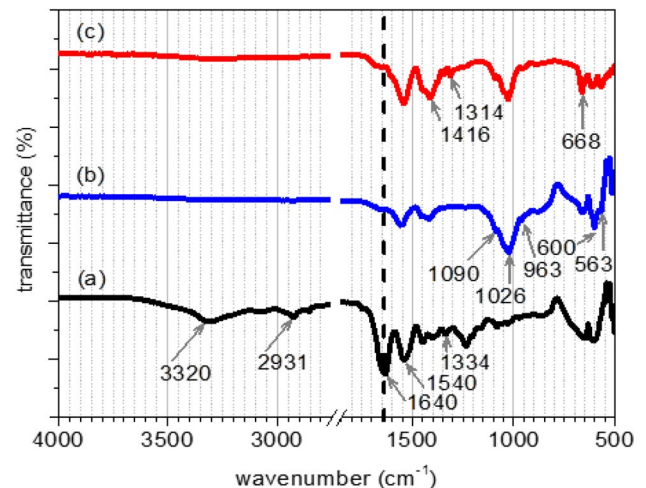


**Fig. 4** IR spectra displaying the functional groups of scaffolds **a** Col **b** Col-HApC **(c)** Col-HApS. Dark dash line indicates a redshift of Amide I ( $1640 \text{ cm}^{-1}$ ) and Amide II ( $1540 \text{ cm}^{-1}$ ) groups of Col-HApC and Col-HApS from Col

where  $\rho_{scaffold}$  is the density of the scaffold measured by the mass of the scaffold over the volume of the scaffold.  $\rho_{material}$  is the density of individual materials the scaffold is prepared from ( $\rho_{collagen} = 1.31 \text{ gcm}^{-3}$  and  $\rho_{HAp} = 3.16 \text{ gcm}^{-2}$ ).

Compressive modulus of cylindrical scaffolds ( $n = 5$ ) of equal height and diameter,  $13.8 \pm 0.3 \text{ mm}$  was determined using Rubicon DMG 6160 (Denison Mayes Group). The scaffolds were tested under unidirectional compression load of crosshead speed of about  $0.1 \text{ mm/min}$  with a load cell of  $3 \text{ kN}$  to a strain level of  $70\%$ .

### 2.5 Statistical analysis

One-way analysis of variance (ANOVA) and Tukey's post-hoc test were used to relate the groups. The statistical significance was determined at a confidence level of  $p < 0.05$  and all data presented were averages (mean) with their standard deviations as errors.

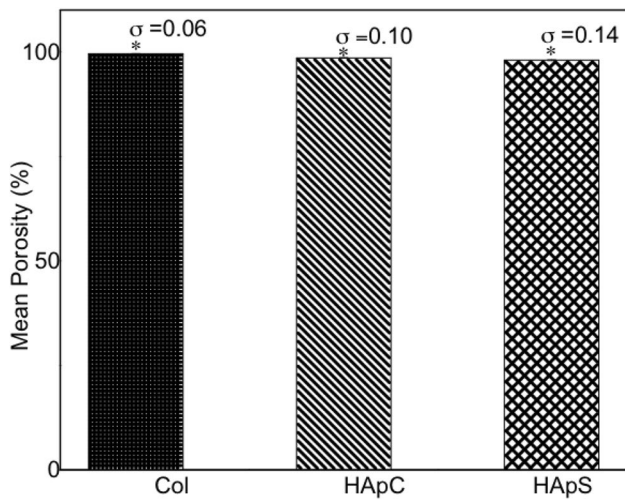
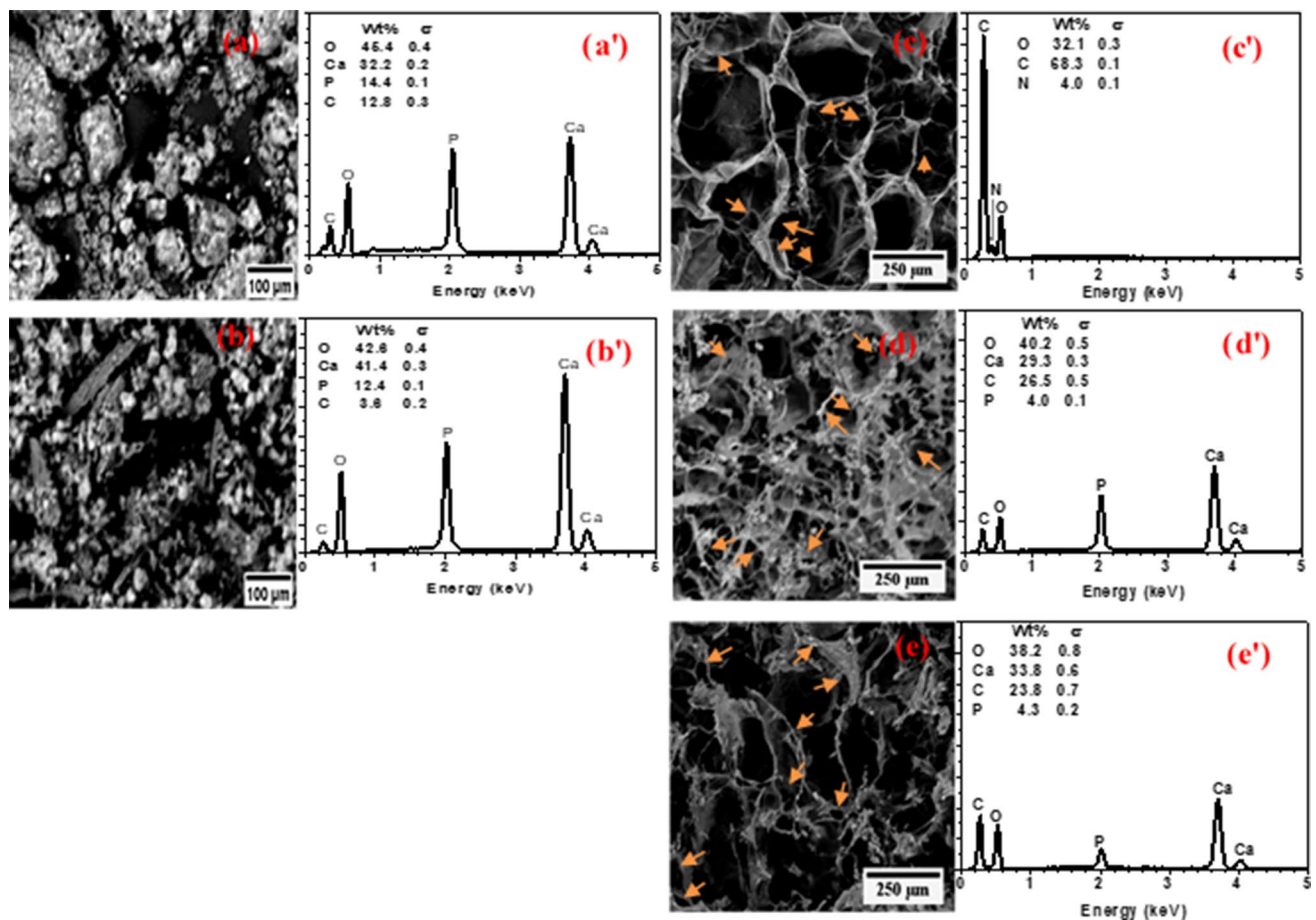


**Fig. 5** Mean porosity of scaffolds. The freeze drying created decimated difference in the scaffolds. \* indicates the statistical significance at  $p < 0.05$  and  $\sigma$  represents the standard deviation

### 3 Results

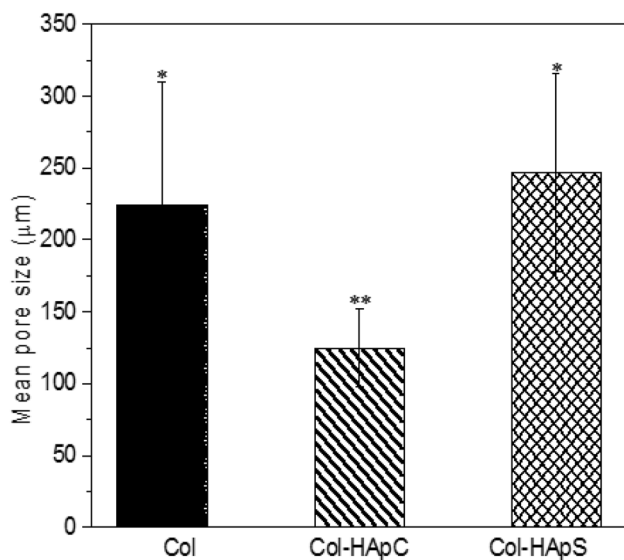
#### 3.1 XRD of HAp and scaffold characterization

Figure 1 shows x-ray diffraction (XRD) patterns of HApC and HApS whereas Fig. 2 displays XRD patterns of Col, Col-HApC and Col-HApS scaffolds. The scan was performed from 5–70° but the most interesting peaks were found at 5–50°. HApC (Fig. 1a) shows a single phase of hydroxyapatite, and HApS comprises mixed phases of calcite and HAp. The unit cell parameters were computed using a non-linear least square refinement program (Unit cell, CCP14). The lattice constants for HApC and HApS were identified to be,  $a = 9.4146 \text{ \AA}$ ,  $c = 9.4157 \text{ \AA}$  and  $a = 9.3804 \text{ \AA}$ ,  $c = 6.8422 \text{ \AA}$ , respectively. The Scaffolds XRD patterns for Col-HApC (Fig. 1b) showed a similar phase to HApC plus broad peaks associated with collagen. Col-HApS (Fig. 1c) showed dual phases of graphitic-like carbon nitride ( $g\text{-C}_3\text{N}_4$ ) and HAp.



**Fig. 6** Shows SEM images of **a** HApC **b** HApS **c** Col **d**, Col-HApC **e** Col-HApS and the corresponding EDS spectra (**a'**, **b'**, **c'**, **d'** and **e'**). The HApC surface comprises agglomerated chunks and small spherical chunks whereas HApS show agglomeration of small

spherical grains and plate-like grains. Scaffolds surface (**c–e**) shows larger and smaller pores with yellow allows indicating pore interconnectivity



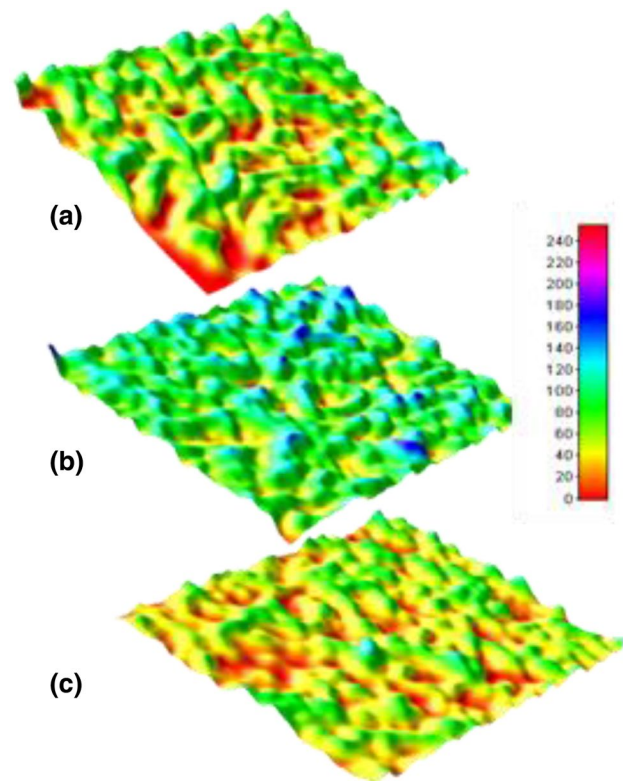
**Fig. 7** Mean pore size of Col, Col-HApC, and Col-HApS scaffolds. \* and \*\* indicates the statistical significance at  $p < 0.05$

### 3.2 IR of HAp and scaffold characterization

Figure 3 shows infrared (IR) spectra of HApC and HApS whereas Fig. 4 shows Col, Col-HApC and Col-HApS scaffolds, respectively. In Fig. 3, the wavenumbers 1090, 1026, 963, 600, and 563  $\text{cm}^{-1}$  correspond to phosphate functional groups of HAp. The wavenumber at 600  $\text{cm}^{-1}$  is the liberational hydroxide group. The fingerprints at wavenumbers 1412 and 871  $\text{cm}^{-1}$  are carbonate groups. In Fig. 4a, the wavenumbers 3320 and 2931  $\text{cm}^{-1}$  are Amide A and Amide B functional groups of Col, respectively. The main collagen groups Amide I, and Amide II are found at wavenumbers 1640 and 1540  $\text{cm}^{-1}$ , respectively and Amide III group occurred at 1334  $\text{cm}^{-1}$ . In Fig. 4b and c, Amide A, Amide B and Amide III groups disappeared but Amide I and Amide II groups are maintained with modifications. Amide I and Amide II groups of HApC and HApS were redshifted to the same wavenumber but the intensity of HApS is higher than that of HApC. HApS in addition is found with new fingerprints that occurs at wavenumbers 1416, 1314 and 668  $\text{cm}^{-1}$  that are comparable to graphitic carbon nitrite ( $\text{g-C}_3\text{N}_4$ ) functional groups.

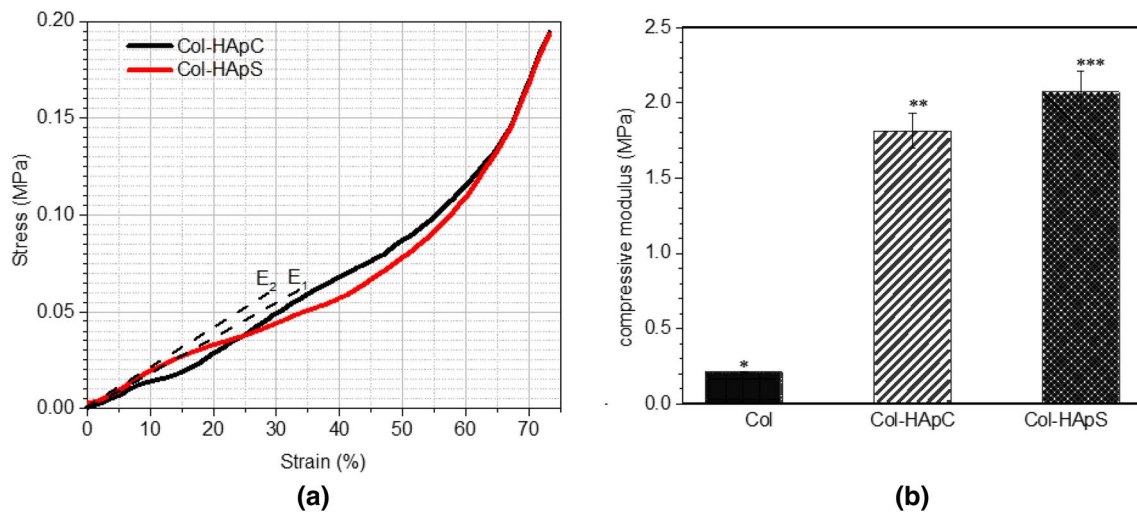
### 3.3 Scaffold porosity, SEM and EDS characterization of HAp and scaffold

Figure 5 shows the mean porosity of the scaffolds. The porosity shows no statistical difference ( $p < 0.05$ ) among scaffolds. The mean porosity in percentage for Col, Col-HApC, and Col-HApS are  $99.5 \pm 0.06$ ,  $98.5 \pm 0.11$ , and  $98.0 \pm 0.14$ , respectively.



**Fig. 8** Interactive 3D surface plot of scaffolds **a** Collagen **b** Col-HApC **c** Col-HApS. The surface plots were obtained using SEM images in image J. Col-HApS has higher pore depth (red) and better interconnectivity followed by Col and Col-HApC scaffolds

Figure 6 shows the scanning electron microscope (SEM) images and energy dispersive X-ray spectroscopy (EDS) spectra of HApC, HApS and scaffolds. The SEM images of HApC in Fig. 6a shows small spherical and agglomerated chunks and small spherical grains that are irregularly dispersed; HApS Fig. 6b shows rod-like grains together with spheroids. These images and the EDS spectra are typical of commercial hydroxyapatite and carbonated hydroxyapatite [27, 28]. The SEM images in Fig. 6c–e shows larger and smaller pores that are interlinked. The scaffolds pore geometry (pore size and pore interconnectivity) were determined from Fig. 6c–e and presented in Fig. 7. The pure collagen (Col), Col-HApS reveals a mean pore size of  $(224.4 \pm 85.7) \mu\text{m}$  and  $(246.9 \pm 68.7) \mu\text{m}$ , respectively. The single ANOVA post hoc statistics indicated no statistical difference between Col and Col-HApS. However, the mean pore size of Col-HApC  $(125.5 \pm 26.7) \mu\text{m}$  is about half that of Col-HApS mean pore size. Pore interconnectivity is indicated with yellow arrows on the images surface shows how voids or pores are interlinked to each other within the scaffolds. It was found that the pores on the pore walls (wall pores) were smaller than the main pores on the scaffold surfaces. The mean size of the wall pores



**Fig. 9** **a** Stress–strain curve and **b** compressive modulus of scaffolds. The linear portion in **a** indicated as  $E_1$  and  $E_2$  were used to determine the compressive modulus of Col–HApC and Col–HApS,

was  $(60.3 \pm 22.9)$ ,  $(22.3 \pm 8.4)$  and  $(64.7 \pm 29.1)$   $\mu\text{m}$  for Col, Col–HApC and Col–HApS, respectively. The surface topology of Col–HApS indicated as yellow in Fig. 8c confirm the ease of maneuvering through pores. The surface topology is more akin to Col (Fig. 8a) as compared to Col–HApC (Fig. 8b) and this supports the view that channels exist between the main pores through the wall pores. The observation suggests that the wall pores will enhance pore interconnectivity.

### 3.4 Compressive modulus

Figure 9a and b represents the stress–strain curve and compressive modulus of Col–HApC, Col–HApS and Col scaffolds. The slope of the linear portion of the curve within 10% of the strain axis was used to determine the compressive modulus of the scaffolds indicated in Fig. 9b. The modulus of Col, Col–HApC, and Col–HApS were  $20.8 \pm 0.4$  kPa,  $181.2 \pm 11.8$  kPa, and  $206.9 \pm 14.1$  kPa, respectively.

## 4 Discussion

The characterization (XRD, FTIR, SEM and EDS) confirms that HApC and HApS are hydroxyapatite (HAp) and carbonated hydroxyapatite (CHAp) plus (+) calcite respectively. The lattice constants for HApC and HApS correspond to a unit cell volume of  $527.6838 \text{ \AA}^3$  and  $521.3976 \text{ \AA}^3$ , respectively. The unit cell volumes are in line with the theoretical and experimental values

respectively. Col–HApS is stiffer followed by Col–HApC and Col. \*, \*\*, and \*\*\* indicates the statistical significance at  $p < 0.05$

reported by Astala and Stott [29]. Their work reports a smaller decrease in the unit cell volume between 1–2% of HAp for CHAp at B-site substitution. The decrease of the unit cell volume of HApS by 1.19% as compared to the unit cell volume of HApC suggests that HApS underwent  $\text{CO}_3^{2-}$  substitution where  $\text{CO}_3^{2-}$  occupied  $\text{PO}_4^{3-}$  site (B-site).  $\text{CO}_3^{2-}$  could substitute at B-site and or OH<sup>-</sup> site (A-site) in HAp depending on the thermodynamic conditions and how charges are compensated. For HApS,  $\text{Ca}^{2+}$  was given out for charge compensation, and because  $\text{CO}_3^{2-}$  has a smaller ionic size, it is oriented at B-site parallel to the c-axis of the hexagonal unit cell for stability and that results in a reduced unit cell volume.

The Col interaction with HApC has been modelled by Cutini, Michele et al. [30] using ab initio simulation. The mechanism of interaction is through adsorption of the amide I bonds (C=O) of Col proline molecules and the exposed  $\text{Ca}^{2+}$  and electrostatic interactions as illustrated in Fig. 10b. The redshift of the amide I and II bonds are the evidence of strong interaction between Col and HApC. The amide A, amide B, and amide III peaks were altered and the surface of the HApC modified through conformation changes assisted by protonation (from the acetic acid).

Col adsorption to HApS surface depended on the  $\text{CO}_3^{2-}$  substitution at the B-site of HApS. The available way for Col to bind with HApS is through the amide I (C=O) and  $\text{CO}_3^{2-}$  as shown in Fig. 10c. The Col proline molecules interaction with HApS is initiated through protonation similar to Col and HApC interaction in the acetic acid environment. For stability, C=O and  $\text{CO}_3^{2-}$  interacted through E-Z stereoisomerism. The interaction is restricted and resulted in a new geometrical configuration which

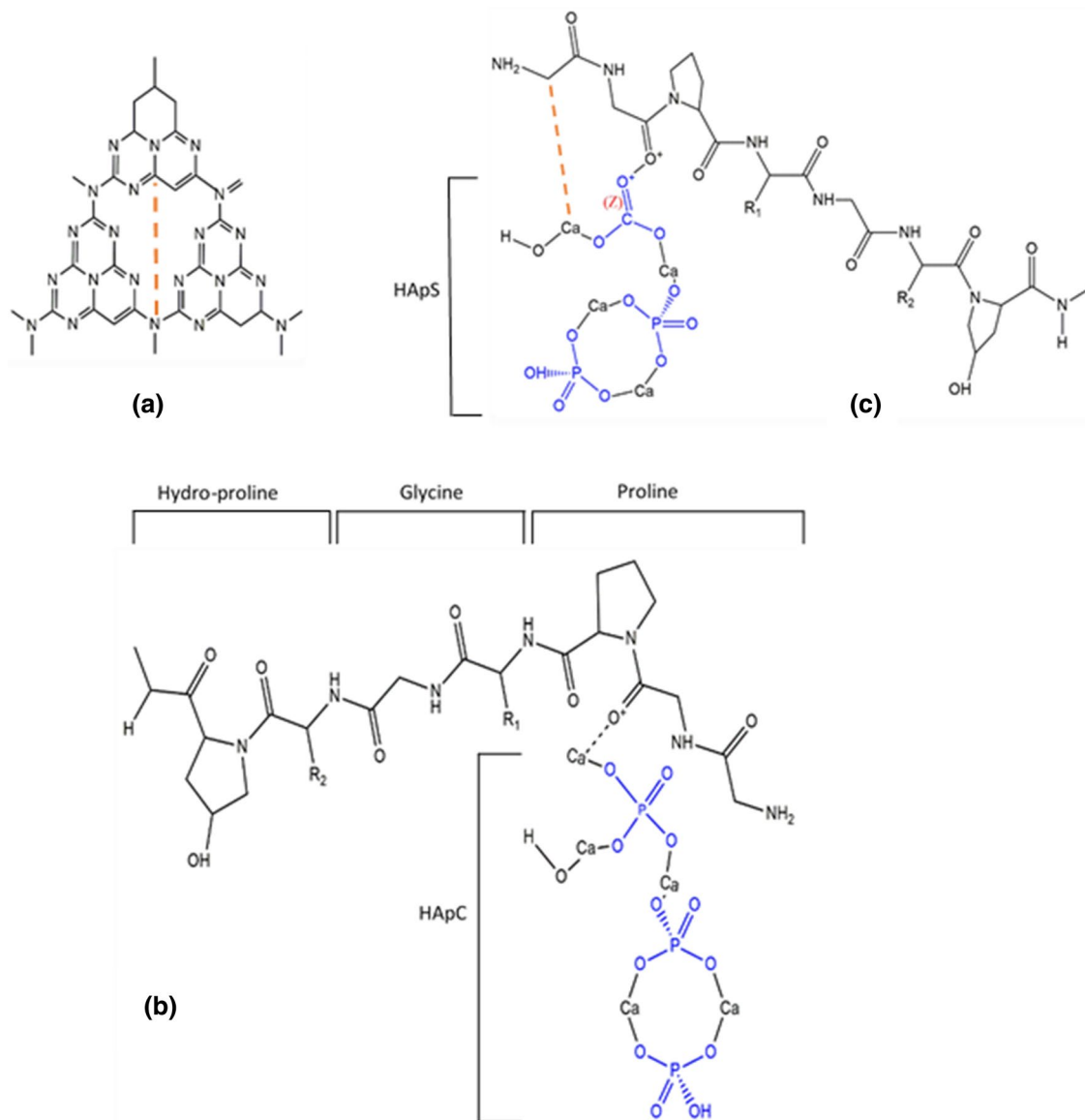


**Fig. 10** Molecular structure of **a** tri-s-triazine  $g-C_3N_4$  **b** Col-HApC **c** Col-HApS. The structures were drawn using cheigmdraw Pro 12.0. Solid long bond lengths represent bonds in a plane. Dash (broken) wedge bonds represents bonds disappearing away from the

viewer. The Z in **c** indicates E-Z stereoisomerism and that produced the solid short bond lengths. The red dash lines indicate similar interplanar distance between the two structures (**a**) and (**c**)

produced shorter planar bond lengths. The structure is comparable to the partial tri-s-triazine  $g-C_3N_4$  polymeric structure as revealed by XRD in Fig. 2c and IR in Fig. 4c. The observation was absent in Col-HApC, and this confirms that the  $g-C_3N_4$  phase in Col-HApS was due to the presence of the HApS in Col-HApS. Doblinger et al. [31] and Federica et al. [32], report XRD patterns of partial tri-s-triazine  $g-C_3N_4$  polymeric structure and the peaks are comparable to  $9.2^\circ$ ,  $13.7^\circ$  and  $27.6^\circ$  positions as indicated in Fig. 2c. The peak positions correspond to (100), (101), and (002) plane, respectively. The (002) plane is the most intense reflection of  $g-C_3N_4$  but because Col interacted

with HApS at the same reflection, it is expected that the peak intensity reduced and becomes lower than those at lower angles. This interaction produced the partial formation of the tri-s-triazine  $g-C_3N_4$  polymeric structure. FTIR in Fig. 4c confirms the phase. The main functional group of fully formed tri-s-triazine  $g-C_3N_4$  occurs at  $808\text{ cm}^{-1}$  [33] and that of partial tri-s-triazine  $g-C_3N_4$  occurs around  $668\text{ cm}^{-1}$  [34]. The latter functional group position is the same as reported in this study. The tri-s-triazine  $g-C_3N_4$  is a layered structure and influenced the pore geometry and the stiffness.



The pore geometry was influenced to an extent that it resulted in a larger mean pore size with better pore interconnectivity in Col-HApS as demonstrated in Figs. 8 and 9. Although, larger pore size is essential for effective cell permeability and nutrient transport in a scaffold, the sufficient requirement is how the larger pores are interlinked (interconnected) to each other through the pore wall in the scaffold. Pore interconnectivity brings heterogeneity for cellular activities in the scaffold like faster oxygen and nutrient transport, and easy removal of waste by products. This thus, permits faster cellular activities (migration and proliferation), wider range of orientation of cells in the early stages and subsequently infiltration of the cellular ECM of the desired tissue formed. The heterogeneity in Col and Col-HApS will be better due to their high pore interconnectivity than in Col-HApC.

The compressive testing performed indicated statistically ( $p < 0.05$ ) higher stiffness value in Col-HApS than that of Col-HApC. The high stiffness noticed was caused by the presence of the  $g\text{-C}_3\text{N}_4$  phase in the scaffold. The Col-HApS interactions produced a linear structure (Fig. 10b) whereas Col-HApC showed a branched structure (Fig. 10c). The linear chain molecular structure is more reactive than the branched molecular structure and have a stronger interaction with itself. This produces high mechanical stresses on the network chains of the scaffold without affecting porosity. High stiffness is required to promote cell adhesion for proliferation to initiate through the pores. The most intriguing issue is that, most of the processing methods of maximizing stiffness results in reduction in scaffold pore volume (porosity). Notwithstanding, the results from this study demonstrates that the stiffness of the scaffolds depended on scaffold structural network architecture but not necessarily on the inverse relation to the porosity, as usually reported. There was no major significant difference in the scaffolds mean porosities values in Fig. 5, but the minute changes translated to a major difference in stiffness. This finding is important since advanced biomaterials could be developed using microstructure manipulations to achieve high stiffness in highly interconnected porous materials. Similar concept is reported where Cu is introduced into Zn bone implants and through heterogeneous nucleation, peritectic phase evolved which enhanced the mechanical properties of the implant [35]. The large pore size, high pore interconnectivity and high stiffness of the advanced scaffold (Col-HApS) fabricated will have greater potential for different tissues to elicit its ECM for bone regeneration.

## 5 Conclusion

Bone tissue 3D scaffolds were fabricated from 30% type 1 collagen (Col) and 70% snail shell hydroxyapatite (HApS) using freeze-drying suspension method. The scaffold pore geometry and compressive modulus (stiffness) were compared to that of collagen (Col) alone, and Col-commercial hydroxyapatite (Col-HApC) scaffolds. The mean pore size of Col-HApS scaffold was, ( $246.9 \pm 68.7 \mu\text{m}$ ), which is statistically ( $p < 0.05$ ) same as the mean pore size of Col scaffolds ( $224.4 \pm 85.7 \mu\text{m}$ ) but larger than Col-HApC scaffolds ( $125.5 \pm 26.7 \mu\text{m}$ ). The larger pore size of Col-HApS arises from the  $\text{CO}_3^{2-}$  substitution at the B-site of HApS that underwent stereoisomerism and formed a geometrical configuration that was comparable to partial tri-s-triazine graphitic-like carbon nitride polymeric structure. The structure is layered with an interconnected large pore structure and that influenced the scaffold. The stiffness of Col-HApS ( $206.9 \pm 14.1 \text{ kPa}$ ) was statistically ( $p < 0.05$ ) higher than the stiffness of Col ( $20.8 \pm 0.4 \text{ kPa}$ ) and Col-HApC ( $181.2 \pm 11.8 \text{ kPa}$ ). The observed higher stiffness values of Col-HApS were attributed to the linear geometrical shape of collagen molecules that permitted more interaction with HApS crystals. The Col-HApS fabricated has improved pore geometry and stiffness and could be therefore be used in bone tissue regeneration as compare to Col and Col-HApC. Also, the results demonstrated that microstructural manipulations could be used to improve scaffold stiffness without altering porosity.

**Acknowledgements** The author acknowledged Emmanuella Essilfie, student of University of Ghana Medical School, Korle-Bu, Ghana and Honey, Anim-Ayeko, Teaching Assistant, Department of Biomedical Engineering, University of Ghana, Ghana for their support during the HApS preparation. We also appreciate the help provided by Mu-Huan Lee and Sasza Chyntara Nabilla, DPhil scholars, Biomaterials Group, Department of Materials, University of Oxford during compressive testing of the scaffolds.

## Compliance with ethical standards

**Conflict of interest** The authors have no conflict of interest to declare.

## References

1. Wahl DA, Czernuszka JT (2006) Collagen-hydroxyapatite composites for hard tissue repair. *Eur Cells Mater* 11:43–56. <https://doi.org/10.22203/eCM.v011a06>
2. Amini AR, Laurencin CT, Nukavarapu SP (2012) Bone tissue engineering: recent advances and challenges. *Crit Rev Biomed Eng* 40:363–408
3. Upadhyay RK (2017) Role of calcium bio-minerals in regenerative medicine and tissue engineering. *J Stem Cell Res Ther* 2:00081. <https://doi.org/10.15406/jsrt.2017.02.00081>

4. Wade RJ, Burdick JA (2012) Engineering ECM signals into biomaterials. *Mater Today* 15:454–459. [https://doi.org/10.1016/S1369-7021\(12\)70197-9](https://doi.org/10.1016/S1369-7021(12)70197-9)
5. Ahadian S, Khademhosseini A (2018) Smart scaffolds in tissue regeneration. *Regen Biomater* 5:125–128. <https://doi.org/10.1093/rb/rby007>
6. Parisi L, Toffoli A, Ghiacci G, Macaluso GM (2018) Tailoring the interface of biomaterials to design effective scaffolds. *J Funct Biomater* 9:50. <https://doi.org/10.3390/jfb9030050>
7. Sachlos E, Czernuszka JT (2003) Making tissue engineering scaffolds work. review on the application of solid freeform fabrication technology to the production of tissue engineering scaffolds. *Eur Cells Mater* 5:39–40
8. Thavorniyutikarn B, Chantarapanich N, Sitthiseripratip K, Thouas GA, Chen Q (2014) Bone tissue engineering scaffolding: computer-aided scaffolding techniques. *Prog Biomater* 3:61–102. <https://doi.org/10.1007/s40204-014-0026-7>
9. Carlisle ER, Fischgrund JS (2009) Bone graft and fusion enhancement. In: *Surgical management of spinal deformities*. WB Saunders, pp 433–448
10. Kuhn LT (2001) Bone mineralization. pp 787–794
11. Ghassemi T, Shahroodi A, Ebrahimzadeh MH, Mousavian A, Movaffagh J, Moradi A (2018) Current concepts in scaffolding for bone tissue engineering. *Arch bone Jt Surg* 6:90–99
12. Makareeva E, Leikin S (2014) Collagen structure, folding and function. In: *Osteogenesis Imperfecta*. Academic Press, pp 71–84
13. Perumal S, Antipova O, Orgel JPRO (2008) Collagen fibril architecture, domain organization, and triple-helical conformation govern its proteolysis. *Proc Natl Acad Sci* 105:2824–2829. <https://doi.org/10.1073/pnas.0710588105>
14. Viguet-Carrin S, Garnero P, Delmas PD (2006) The role of collagen in bone strength. *Osteoporos Int* 17:319–336. <https://doi.org/10.1007/s00198-005-2035-9>
15. Turnbull G, Clarke J, Picard F, Riches P, Jia L, Han F, Li B, Shu W (2018) 3D bioactive composite scaffolds for bone tissue engineering. *Bioact Mater* 3:278–314. <https://doi.org/10.1016/j.bioactmat.2017.10.001>
16. Palmer LC, Newcomb CJ, Kaltz SR, Spoerke ED, Stupp SI (2008) Biomimetic systems for hydroxyapatite mineralization inspired by bone and enamel. *Chem Rev* 108:4754–4783. <https://doi.org/10.1021/cr8004422>
17. Liu C, Zhai H, Zhang Z, Li Y, Xu X, Tang R (2016) Cells recognize and prefer bone-like hydroxyapatite: biochemical understanding of ultrathin mineral platelets in bone. *ACS Appl Mater Interfaces* 8:29997–30004. <https://doi.org/10.1021/acsami.6b10374>
18. Perez RA, Mestres G (2016) Role of pore size and morphology in musculo-skeletal tissue regeneration. *Mater Sci Eng C* 61:922–939. <https://doi.org/10.1016/j.msec.2015.12.087>
19. Chocholata P, Kulda V, Babuska V, Chocholata P, Kulda V, Babuska V (2019) Fabrication of scaffolds for bone-tissue regeneration. *Materials (Basel)* 12:568. <https://doi.org/10.3390/ma12040568>
20. Murphy CM, O'Brien FJ (2010) Understanding the effect of mean pore size on cell activity in collagen-glycosaminoglycan scaffolds. *Cell Adhes Migr* 4:377–381. <https://doi.org/10.4161/cam.4.3.11747>
21. Yu L, Rowe DW, Perera IP, Zhang J, Suib SL, Xin X, Wei M (2020) Intrafibrillar mineralized collagen-hydroxyapatite-based scaffolds for bone regeneration. *ACS Appl Mater Interfaces* 12:18235–18249. <https://doi.org/10.1021/acsami.0c00275>
22. Shuai C, Cheng Y, Yang W, Feng P, Yang Y, He C, Qi F, Peng S (2020) Magnetically actuated bone scaffold: microstructure, cell response and osteogenesis. *Compos Part B Eng*. <https://doi.org/10.1016/j.compositesb.2020.107986>
23. Zhu B, Zhang L, Cheng B, Yu J (2017) First-principle calculation study of tri-s-triazine-based g-C<sub>3</sub>N<sub>4</sub>: a review. *Appl Catal B Environ* 224:983–999. <https://doi.org/10.1016/j.apcatb.2017.11.025>
24. Cao Q, Kumru B, Antonietti M, Schmidt BVKJ (2020) Graphitic carbon nitride and polymers: a mutual combination for advanced properties. *Mater Horizons* 7:762–786. <https://doi.org/10.1039/c9mh01497g>
25. Adak MD, Purohit KM (2011) Synthesis of nano-crystalline hydroxyapatite from dead snail shells for biological implantation. *Trends Biomater Artif Organs* 25:101–106
26. Asimeng BO, Fianko JR, Kaufmann EE, Tiburu EK, Hayford CF, Anani PA, Dzikuoku OK (2018) Preparation and characterization of hydroxyapatite from *Achatina achatina* snail shells: effect of carbonate substitution and trace elements on defluorination of water. *J Asian Ceram Soc*. <https://doi.org/10.1080/21870764.2018.1488570>
27. Trinkūnaitė-Felsen J (2014) Investigation of calcium hydroxyapatite synthesized using natural precursors. Vilnius University
28. Pareja NM, Escobar DM, Ossa CP, Echavarría A (2008) Synthesis and characterization of microporous hydroxyapatite, comparison with a commercial product. *Rev Fac Ing* 43:67–76
29. Astala R, Stott MJ (2005) First principles investigation of mineral component of bone: CO<sub>3</sub> substitutions in hydroxyapatite. *Chem Mater* 17:4125–4133. <https://doi.org/10.1021/cm050523b>
30. Cutini M, Corno M, Costa D, Ugliengo P (2019) How does collagen adsorb on hydroxyapatite? Insights from Ab initio simulations on a polyproline type II model. *J Phys Chem C* 123:7540–7550. <https://doi.org/10.1021/acs.jpcc.7b10013>
31. Döblinger M, Lotsch BV, Wack J, Thun J, Senker J, Schnick W (2009) Structure elucidation of polyheptazine imide by electron diffraction—a templated 2D carbon nitride network. *Chem Commun* 12:1541–1543. <https://doi.org/10.1039/b820032g>
32. Fina F, Callear SK, Carins GM, Irvine JTS (2015) Structural investigation of graphitic carbon nitride via XRD and neutron diffraction. *Chem Mater* 27:2612–2618. <https://doi.org/10.1021/acs.chemmater.5b00411>
33. Zhang W, Zhou L, Shi J, Deng H (2018) Synthesis of Ag<sub>3</sub>PO<sub>4</sub>/G-C<sub>3</sub>N<sub>4</sub> composite with enhanced photocatalytic performance for the photodegradation of diclofenac under visible light irradiation. *Catalysts* 8:45. <https://doi.org/10.3390/catal8020045>
34. Bojdy MJ (2009) On new allotropes and nanostructures of carbon nitrides
35. Shuai C, Dong Z, He C, Yang W, Peng S, Yang Y, Qi F (2020) A peritectic phase refines the microstructure and enhances Zn implants. *J Mater Res Technol*. <https://doi.org/10.1016/j.jmrt.2020.04.037>

**Publisher's Note** Springer Nature remains neutral with regard to jurisdictional claims in published maps and institutional affiliations.